A 2-D Space-Variant Chirp Scaling Algorithm Based on the RCM Equalization and Subband Synthesis to Process Geosynchronous SAR Data

Guang-Cai Sun, *Member, IEEE*, Mengdao Xing, *Member, IEEE*, Yong Wang, Jun Yang, and Zheng Bao, *Life Senior Member, IEEE*

***Abstract*—A space-variant chirp scaling algorithm based on the range cell migration (RCM) equalization and azimuth subband synthesis has been studied to process simulated geosynchronous synthetic aperture radar (GEO-SAR) data. The acceptable order of terms in polynomials for the slant range models in the RCM correction and phase error compensation, division of subband, and suppression of grating lobes of the subbands was investigated. Qualitatively and quantitatively, the method was able to focus simulated GEO-SAR signals well. Finally, the constraint on the spatial extent of azimuth and range dimensions using the algorithm was assessed.**

***Index Terms*—Azimuth subband division and synthesis, geosynchronous synthetic aperture radar (GEO-SAR), range cell migration (RCM) equalization, 2-D space variant.**

I. Introduction

DIFFERENT from low-Earth-orbit spaceborne synthetic aperture radar (SAR) constellations [1]–[3] that are used to improve temporal resolution in data acquisition, a geosynchronous SAR (GEO-SAR) at an orbit height near 36 000 000 m above the Earth surface is capable of acquiring data with a wide ground swath and at a short revisit cycle [4]–[7]. One GEO-SAR can provide daily coverage for approximately 1/3 of the globe [8]. A target of interest such as an area after a disastrous event can even be imaged 1.5–2.5 h per day [9]. Therefore, the GEO-SAR, as a complement to low-Earth-orbit spaceborne SARs, can provide critical high-temporal resolution data sets that are invaluable in search and rescue missions (http://www.sarsat.noaa.gov/, http://www.cospas-sarsat.org/, and http://www.uscg.mil/hq/g-o/g-opr/sar.htm) and disaster monitoring and assessment. Currently, the GEO-SAR research includes the design of the SAR antenna and system parameters [10] and the understanding of the atmospheric effect on the imaging [11]. Imaging algorithms to process the GEO-SAR data are generally lagging. A signal model for the GEO-SAR with the approximation of the two-way slant range as the third-order series of slow time has been studied [12]. However, the slant range of the SAR is more complex than what the third-order series can handle [13]. Also, the range cell migration (RCM) correction method in the azimuth-time domain used in [12] is not effective for the correction of all azimuth point targets.

Zhou *et al.* [13] have analyzed the slant range model and have adopted the back projection algorithm (BPA) to process GEO-SAR data in the time domain. However, with respect to efficiency, the algorithms in the range-Doppler (RD) domain that include the chirp scaling (CS) algorithms [14], [15] are good choices. Thus, an algorithm further developed in the RD domain retains not only the high efficiency but also nearly the same processing scheme that traditional RD algorithms have. Moreover, modification of a current hardware and software module or development of a new replacement should be easy, which makes the algorithm development in the RD domain attractive.

In this paper, a new 2-D space-variant CS algorithm (SV-CSA) to focus the GEO-SAR signal is studied. First, the slant range signal model without the "stop–go" assumption of slow time is used [12], [16]. Then, the slant range history for the RCM correction is modeled as a third-order polynomial and the phase history for phase correction up to the sixth-order terms. Differing from a traditional range model, the slant range model is azimuth and range variant or 2-D space variant. Because the slant range histories of different azimuth targets within a range cell are azimuth variant, the uniform RCM correction function derived from a reference target within the cell could not be used to correct the RCMs for nonreference targets satisfactorily. An RCM equalization operation is then applied to the azimuth-variant RCMs of individual targets within one range cell. The resulting RCMs of the targets are azimuth invariant and are corrected uniformly. Because the accuracy requirement in range for the phase error compensation is much higher than that for the RCM correction, a frequency band division and then a synthesis method of the azimuth signal in the RD domain are further developed. After the division, a set of phase functions updated with different subbands is utilized to compensate for phase errors caused by azimuth variants in individual subbands. Then, the subband signals are synthesized into an integrated signal that is well focused.

Manuscript received March 1, 2012; revised August 29, 2012, March 31, 2013, and August 30, 2013; accepted October 4, 2013. This work was supported in part by the National Natural Science Foundation of China under Grants 61222108 and 61301292, by the "973" Program of China under Grant 2010CB731903 to the Xidian University of China, and by the USGS/AmericaView to East Carolina University of USA under Grant 211654.

G.-C. Sun, M. Xing, J. Yang, and Z. Bao are with the National Laboratory of Radar Signal Processing, Xidian University, Xi'an 710071, China (e-mail: rsandsgc@126.com).

Y. Wang is with the School of Resources and Environment, University of Electronic Science and Technology of China, Chengdu 611731, China, and also with the Department of Geography, Planning and Environment, East Carolina University, Greenville, NC 27858 USA.

Color versions of one or more of the figures in this paper are available online at http://ieeexplore.ieee.org.

Digital Object Identifier 10.1109/TGRS.2013.2285721

0196-2892 © 2013 IEEE. Personal use is permitted, but republication/redistribution requires IEEE permission.
See http://www.ieee.org/publications_standards/publications/rights/index.html for more information.

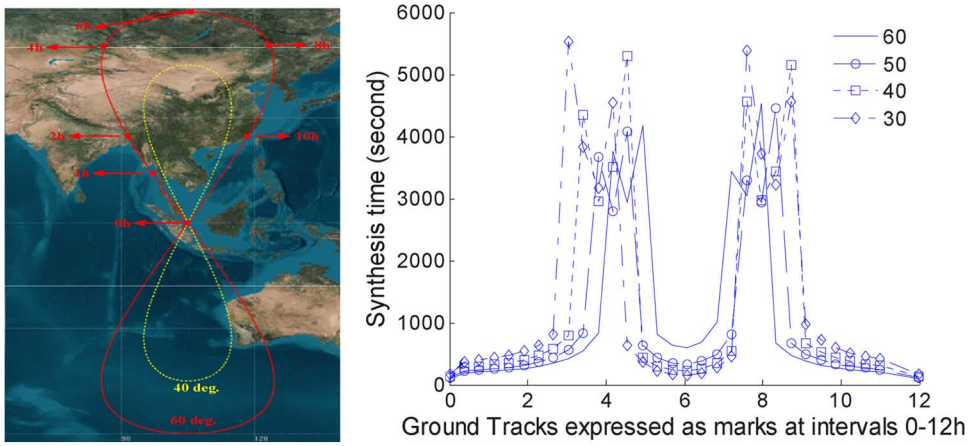

Fig. 1. (a) Ground tracks of GEO-SAR orbits at inclination angles of 40° and 60°. (b) Variable synthesis time along tracks at different inclination angles.

TABLE I
SIMULATION PARAMETERS

Orbit height	36,000,000m	Off-nadir angle	3°
Inclination angle	30-60°	Signal bandwidth	18MHz
Wavelength	0.09m	Slant range resolution	8.33m
Antenna size	40m		

This paper is organized as follows. The space-variant slant range and signal models for the GEO-SAR are analyzed in Section II. In Section III, the modified CS algorithm based on the RCM equalization and subband synthesis is presented. Considerations of algorithm implementation are discussed in Section IV. Validity and applicability are studied in Section V. In Section VI, the conclusion is drawn.

II. SPACE-VARIANT SLANT RANGE AND SIGNAL MODELS FOR GEO-SAR

With available STK software (http://www.agi.com/), elliptical orbits of the GEO-SAR are simulated. As observed at the center of the Earth, the track of the GEO-SAR traveling along its inclined orbit is an "8" curve in space. Drawing lines to connect the SAR and Earth's center position by position, one obtains a set of intersection points on the Earth's surface. After connection of the points, the ground track of "8" is formed [Fig. 1(a)]. For an easy understanding of the GEO-SAR movement, time intervals at 0, 1, 2, 4, 6, 8, and 10 h of the first half of one day (0–12 h) are marked along the ground track at an inclination angle of 60°. The center of the "8" initiates the time (0 h). From Fig. 1(a), the smaller the inclination angle is, the smaller the extension of the "8" track is. Along the track, the synthesis time, defined as the elapse of the start and end times when a point target is illuminated of one full aperture, varies. To illustrate the variation, we simulate the synthesis time of the SAR at inclination angles from 30° to 60°, respectively. With parameters in Table I as inputs to the STK software, the data points of elapses along track of time marks of 0–12 h are plotted [Fig. 1(b)]. The variation is between ∼100 and 5000 s. The time also changes as the inclination angle varies. Finally, at the same inclination angle, the pattern of the synthesis time between 12 and 24 h is the same as that between 0 and 12 h. For the curve of an inclination angle, there are two peaks around 4 and 8 h. Moreover, the peaks move close to each other as the inclination angle increases.

Because the SAR moves significantly during a cycle of one transmitted and received signal, a slant range model with the traditional "stop–go" assumption is no longer valid. The range model without the assumption [12], [16] is used. Therefore, when the instantaneous Doppler frequency of target P is zero, the instantaneous slant range at t_a can be formulated as

$$R_p(t_a)=\frac{R_T(t_a)+R_R(t_a)}{2}=R_b+\sum_{n=2}^{N}k_n(t_a-t_c)^n+\cdots \quad (1)$$

where $R_T(t_a)$ is the distance from the SAR transmitter to a ground target and $R_R(t_a)$ represents the distances between the target and SAR receiver. R_b is the nearest slant range. t_c is zero-Doppler time. Methods including Chebyshev, Legendreand, and Taylor polynomials [17]–[19] can be used to express k_n. Here, the Taylor polynomial is utilized. In this case, $k_n=(1/n!)(d^nR_p(t_a)/dt_a^n)|_{t_a=t_c}$ denotes the n-th order derivative at $t_a=t_c$. In general, $k_n=k_n(t_c,R_b)$ is space variant.

It is well known that a range model with a set of fixed parameters k_n is typically used to represent azimuth targets within one range cell. However, the model cannot adequately address the azimuth-variant characteristics of the targets inside one range cell of the GEO-SAR data. If the model were applied, an unacceptable difference in slant ranges would result. To quantify the difference caused by the azimuth variant, we performed another simulation with parameters in Table I. The center time was at the latitude of 4 h [Fig. 1(a)]. The inclination angle was 60°. Two targets in one range cell and within one synthetic aperture offset were simulated. Slant ranges from the targets were shown in Fig. 2(a), where the curves are subtracted by the minimum value. When the synthesis time was from −420 to 420 s [Fig. 2(b)], the difference was up to ∼180 m or 22 slant range cells (Table I; even though the targets were in the same range cell). To reduce the difference or error, we introduce a new slant range model with k_n being 2-D space variant explicitly.

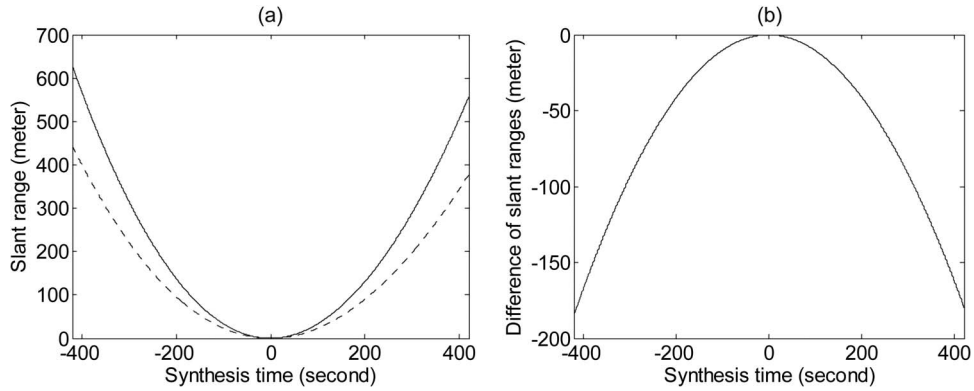

Fig. 2. (a) Two simulated slant ranges and (b) their difference.

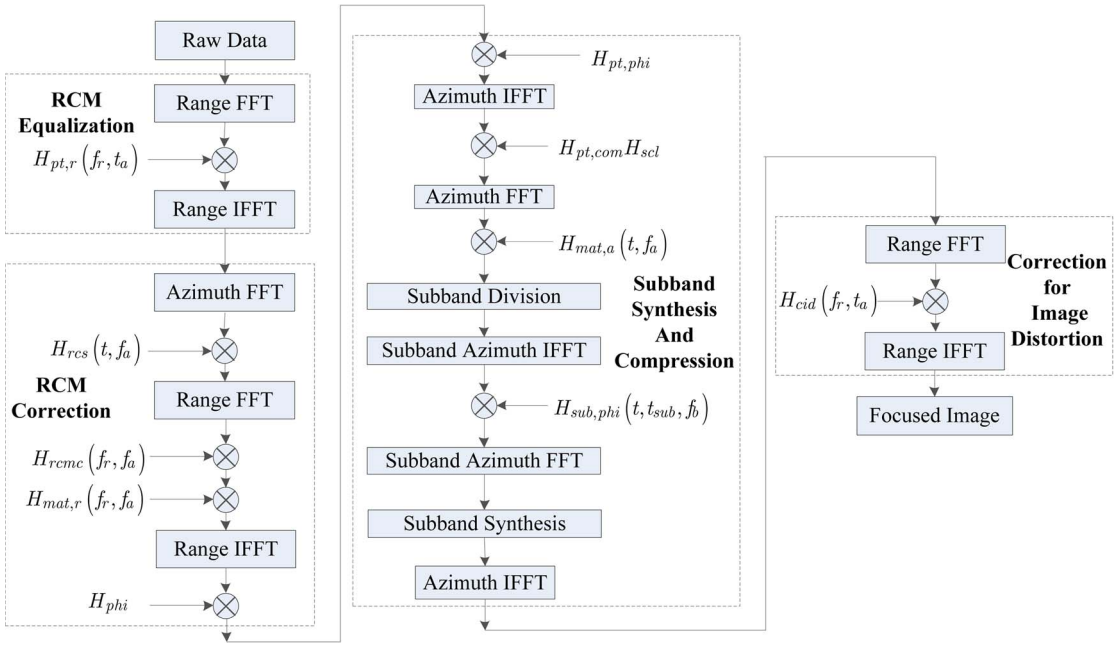

Fig. 3. Flowchart of the algorithm.

Suppose that the transmitted signal is linearly modulated in frequency. The received signal in the range-frequency domain is

$$s(f_r,t_a)=\text{rect}\left[\frac{f_r}{\gamma T_p}\right]w_{az}(t_a-t_c)\times\exp\left(-j\frac{4\pi}{c}(f_c+f_r)R_p(t_a)-j\pi\frac{f_r^2}{\gamma}\right)\quad(2)$$

where c is the speed of light, T_p is the pulse duration, and γ is the frequency modulate rate. rect$[\cdot]$ and $w_{az}(t_a)$ are rectangle and azimuth window functions, respectively. f_r and f_c denote range frequency and carrier frequency. Since $R_p(t_a)$ is space variant, the RCMs of azimuth targets within one range cell are different. Thus, a new 2-D SV-CSA on the basis of the RCM equalization and azimuth subband synthesis is introduced to analyze the space-variant signals of the GEO-SAR. It should be noted that the SV-CSA differs from that in [20]. A SVD-Stolt method is used to deal with the signal that is range variant but azimuth invariant [20].

III. Algorithm

Because the signal is 2-D space variant, the corresponding coefficients in (1) are space variant as well. They can be expressed as a series of the range time and zero-Doppler time. With these considerations, a 2-D SV-CSA is proposed. The algorithm consists of four major steps, namely, RCM equalization, RCM correction, azimuth subband synthesis and compression, and correction for image distortion (Fig. 3). Compared to a traditional CS algorithm, the increased level of complexity in the new algorithm is caused by the long and variable synthetic time for one full synthetic aperture and the highly nonlinear imaging geometry of the GEO-SAR. Each major step is detailed next.

A. RCM Equalization

Azimuth-variant targets located differently in azimuth at the same slant range distance can have variable curvatures of their RCM curves in the azimuth-time domain [Fig. 4(a)]. In

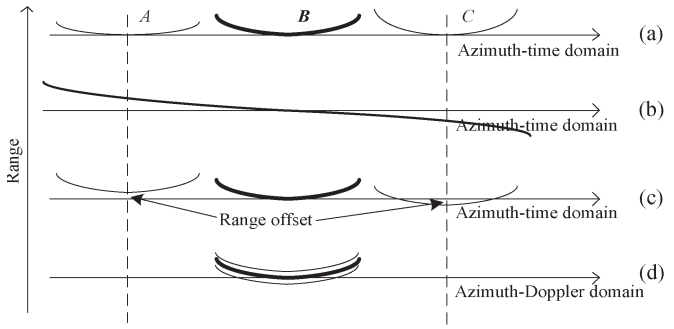

Fig. 4. RCM equalization. (a) Three RCM curves with different degrees of curvature. (b) Range perturbation function. Equalized RCM curves (c) in the azimuth-time domain and (d) in the azimuth-Doppler domain.

the figure, there are targets A, B, and C, with B being the reference target. If signals are transformed into the azimuth-Doppler domain, the RCM curves of the targets are not exactly overlapped. Then, a uniform RCM correction derived from B cannot correct the RCMs of A and C satisfactorily. Components of the second-order and higher order terms in the RCMs remain.

For the acceptable correction of the azimuth-variant RCMs, the RCM equalization with a range perturbation function [Fig. 4(b)] in the azimuth-time domain is proposed. After applying the perturbation function in Fig. 4(b) to the curvatures of Fig. 4(a), one can obtain three RCM curves with similar curvatures [Fig. 4(c)]. The curvatures should be identical if the used function is perfect. Then, a uniform RCM correction can be used to remove the RCMs with the accuracy level at a fraction of range cell resolution [Fig. 4(d)]. The derivation of the function is given next.

The errors caused by RCM components of the fourth-order and higher order terms are generally small. Ignoring the fourth-order and higher order terms, we formulate the range perturbation function in the azimuth-time domain [Fig. 4(b)] as

$$H_{pt,r}(f_r, t_a) = \exp\left(-j\frac{4\pi}{c}(f_c + f_r) r_{pt}(t_a)\right) \tag{3}$$

with

$$r_{pt}(t_a) = A_3 t_a^3 + A_4 t_a^4. \tag{3.a}$$

From (3.a), the range perturbation function is modeled as a polynomial function with coefficients A_3 and A_4 (the selection of the third- and fourth-order terms for $r_{pt}(t_a)$ is justified in Section IV. A_3 and A_4 are solved in Appendix A). Then, multiplying (3) to (2), transforming the result into the range-frequency and azimuth-Doppler domain by using the principle of stationary phase (POSP) [21], [22], we can approximate the phase of the signal as the series of range frequency

$$s(f_r, f_a) \approx \text{rect}\left[\frac{f_r}{\gamma T_p}\right] W_{az}(f_a) \times \exp\left(j\varphi_0 - j2\pi f_a t_c - j2\pi\tau(R_b, f_a) f_r - j\pi\frac{f_r^2}{\gamma_e}\right) \tag{4}$$

with

$$\varphi_0 = D_0 - j\frac{\pi^2}{D_2}\left(f_a - \frac{D_1}{2\pi}\right)^2 + j\sum_{n=3}^{6}\frac{D_n}{D_2^n}\pi^n\left(f_a - \frac{D_1}{2\pi}\right)^n \tag{4.a}$$

$$\tau(R_b, f_a) = -\frac{D_0}{2\pi f_c} - \frac{\pi}{2D_2}\frac{f_a^2}{f_c} + \sum_{n=3}^{6}(n-1)\frac{\pi^{n-1}D_n}{2D_2^n}\frac{f_a^n}{f_c} \tag{4.b}$$

$$\frac{1}{\gamma_e} = \frac{1}{\gamma} + \frac{\pi}{D_2}\frac{f_a^2}{f_c^2} - \sum_{n=3}^{6} n(n-1)\frac{\pi^{n-1}D_n}{2D_2^n}\frac{f_a^n}{f_c^2} \tag{4.c}$$

where $W_{az}(f_a)$ denotes azimuth window function in the Doppler domain and f_a is the azimuth frequency. $D_n = -(4\pi(k_n + r_n)/\lambda)$ (λ denotes wavelength), and $r_n = (1/n!)(d^n r_{pt}/dt_a^n)|_{t_a = t_c}$. φ_0 is the azimuth phase function and is related to the azimuth focusing. $\tau(R_b, f_a)$ is the RCM. γ_e is the equivalent frequency-modulated rate and is linked to the CS function. φ_0, $\tau(R_b, f_a)$, and γ_e are space variant because they are functions of D_n or k_n. However, because γ_e is of weak range variant within an illuminated scene (Appendix B), we can use (B.4) to approximate it. In addition, the third-order phase term of range frequency ignored in (4) is

$$\exp\left(j\frac{\pi^2 f_a^2}{D_2}\frac{f_r^3}{f_c^3} - j\sum_{n=3}\frac{D_n\pi^n f_a^n}{D_2^n}\frac{1}{6}n(n-1)(n+1)\frac{f_r^3}{f_c^3}\right).$$

The values of the third-order phase term with difference inclination angles between 30° and 60° vary from 10^{-2} to 10^{-3} (rad), when the bandwidth is 80 MHz. The values decrease as the inclination angles decrease. The main reason is that the curvature of the SAR orbit with small inclination angle is big, and thus, the Doppler rate is small. When the synthesis under 1000 s is considered, its azimuth bandwidth is smaller so is the third-order phase.

In order to equalize RCM, the azimuth-variant component of $\tau(R_b, f_a)$ should be minimized as discussed in Appendix A. After the minimization, $\tau(R_b, f_a)$ is approximated as

$$\tau(R_b, f_a) \approx t_0 + t_{\text{con}}(t_c) + \alpha(f_a) + \beta(f_a) r \tag{5}$$

where t_0 is the round-trip time from the nearest slant range. $t_{\text{con}}(t_c)$ denotes a range offset caused by the use of the range perturbation function in the RCM equalization [Fig. 4(c)]. $\alpha(f_a)$ is the RCM at reference range, and $\beta(f_a)$ denotes a range factor of the RCM. Their expressions can be found in Appendix A.

B. RCM Correction Using the Modified CS Function

Because the CS algorithm is traditionally based on the property of azimuth shifting invariant, all azimuth targets have an overlapping RCM in the range-time and azimuth-Doppler domain. However, t_{con} of each azimuth target in (5) causes the property not to be valid. Therefore, the traditional CS algorithm results in errors for azimuth points in such a 2-D space-variant

case. With the range parameter from a reference target, scaling function $H_{\mathrm{rcs}}(t, f_a)$, RCM correction function $H_{\mathrm{rcmc}}(f_r, f_a)$, and range matched function $H_{mat,r}(f_r, f_a)$ can be constructed as in [14]. Here, the range scaling factor is $\alpha_{r,scl} = c\beta(f_a)/2$. After the scaling, range compression, and RCM correction, the signal in the range-time and azimuth-Doppler domain can be written as

$$s(t, f_a) = \mathrm{sinc}\left(t - \left(t_0 + \frac{t_{\mathrm{con}}}{1+\alpha_{r,scl}}\right)\right) W_{az}(f_a) \times \exp\left(j\varphi_0 - j2\pi f_a t_c + j\pi\gamma_e\alpha_{r,scl}(1+\alpha_{rsl})\Delta_t^2\right) \quad (6)$$

where $\Delta_t = (c/2)(t_0 + (t_{\mathrm{con}}/1+\alpha_{r,scl}) - (2R_{\mathrm{ref}}/c))$, t is fast time, and t_{con} represents $t_{\mathrm{con}}(t_c)$. The third phase term of (6) is a phase error after the RCM correction. The error varies with azimuth point targets within a range cell and degrades the focusing of signal in azimuth. From the sinc function of (6), t can be used to substitute $t_0 + t_{\mathrm{con}}/(1+\alpha_{r,scl})$. The substitution can be considered as the modification of the original CS algorithm. Therefore, the phase error can be compensated for using

$$H_{phi}(t, f_a) = \exp\left(-j\pi c^2\gamma_e\alpha_{r,scl}(1+\alpha_{r,scl})(t - 2R_{\mathrm{ref}}/c)^2/4\right). \quad (7)$$

Furthermore, inside the sinc function, $\alpha_{r,scl}$ introduces a residual RCM. If the residual is small (e.g., $\leq$1/2 of one range cell resolution), then the residual RCM as well as $\alpha_{r,scl}$ can be ignored. This approximation is valid when the maximum space-variant scenario is simulated in Section V. The residual RCM is about 1/100 of one range cell resolution, and the related $\alpha_{r,scl}$ is $\sim$0.001. Therefore, the result after phase error compensation can be rewritten as

$$s(t,f_a) \approx \mathrm{sinc}(t-(t_0+t_{\mathrm{con}}))W_{az}(f_a)\exp(j\varphi_0 - j2\pi f_a t_c). \quad (8)$$

In (8), t_{con} exists, which is caused by the RCM equalization. t_{con} produces range distortion and is removed after the azimuth phase function of φ_0 is compensated through the subband synthesis in the azimuth focusing. Thus, to keep the discussions and equations simple, we omit t_{con} in the next section.

C. Subband Synthesis for the Azimuth Focusing

From (4.a), φ_0 in (8) is a function of the azimuth position. φ_0 can be expressed as a series of the azimuth frequency, and the corresponding coefficients of the series are azimuth variant. Because the main azimuth-variant term is the second-order term, a third-order phase perturbation function is introduced to reduce the variation and can be written as

$$H_{pt,phi}(t, f_a) = \exp\left(-j4\pi^4 Y_3 f_a^3/\lambda\right) \quad (9)$$

Y_3 is solved in Appendix C. Because Y_3 is small and satisfies (7) in [23], the point of stationary phase (POSP) is not affected. Thus, using the POSP, we multiply (9) to (8) and IFFT to obtain the signal in the azimuth-time domain as

$$s(t_a) = w_{az}(t_a - t_c)\exp\left(-j4\pi r_{pt}(t_a)/\lambda - j4\pi R_p(t_a)/\lambda - j4\pi Y_3 D_2^3(t_a - t_c)^3/\lambda\right). \quad (10)$$

The first phase term is related to the RCM equalization operation. Although after the operation the RCMs of azimuth targets are considered azimuth invariant at the scale of one range cell, the related phase terms are still azimuth variant due to the azimuth-variant $r_{pt}(t_a)$ at the scale of a 1/8 wavelength. Therefore, further phase compensation is needed. The second phase term in (10) is the phase from the slant range, and the third one is introduced by the phase perturbation function of (9). Since both phase terms up to the fourth order are azimuth variant, a higher order phase scaling function should be able to compensate for the azimuth variant adequately. The compensating and scaling function can be written as

$$H_{\mathrm{com},scl}(t_a) = \exp\left(j4\pi r_{pt}(t_a)/\lambda - j4\pi\left(\sum_{i=2}^{5} E_i t_a^i\right)\Big/\lambda\right) \quad (11)$$

where E_i $(i = 2, 3, 4, 5)$ is derived in Appendix C. The first term in (11) is used to reduce to the phase error caused by the equalization operation for each range cell. As compared to the azimuth scaling function in [24] and [25], the second part of the phase term in (11) is more complicated. Multiplying (11) to (10) and expanding the phase term into a series around t_c, one obtains

$$s(t_a) = w_{az}(t_a - t_c)\exp\left(j\sum_{n=0}^{6} B_n(t_a - t_c)^n\right) \quad (12)$$

with

$$B_n = -\frac{4\pi}{\lambda}(k_n + d_n) \quad \text{if } n \neq 3 \quad \text{or}$$
$$B_n = -\frac{4\pi}{\lambda}\left(k_n + d_n + Y_3 D_2^3\right) \quad \text{if} \quad n = 3 \quad (12.a)$$

where $d_n = (1/n!)(d^n/dt_a^n)(\sum_{i=2}^{5} E_i t_a^i)|_{t_a=t_c}$. After transformation of (12) into the azimuth-Doppler domain, the signal becomes

$$s(f_a) = W_{az}(f_a)\exp\left(jB_0 + j\Phi(f_a) - j2\pi f_a t_c\right) \quad (13)$$

with

$$\Phi(f_a) = -\frac{\pi^2}{B_2}\left(f_a - \frac{B_1}{2\pi}\right)^2 + \sum_{n=3}^{6}\frac{B_n}{B_2^n}\pi^n\left(f_a - \frac{B_1}{2\pi}\right)^n. \quad (14)$$

To focus the azimuth signal, we use B_n of an azimuth reference target, i.e., B_{n0}, to construct the azimuth matched filter. Thus, the filter is

$$H_{\mathrm{mat,a}}(t, f_a) = \exp\left(j\frac{\pi^2}{B_{2_0}}f_a^2 - j\sum_{n=3}^{6}\frac{B_{n_0}}{B_{2_0}^n}\pi^n f_a^n\right) \triangleq \exp\left(-j\Phi_{\mathrm{ref}}(f_a)\right) \quad (15)$$

with $\Phi_{\mathrm{ref}}(f_a)$ being the azimuth phase of the reference target in azimuth frequency. After the multiplication of (15) with (13), the result can be written as

$$s_{\mathrm{aft\_mat}}(f_a) = W_{az}(f_a)\exp(jB_0 - j2\pi f_a t_c + j\Phi_{\mathrm{dif}}(f_a)) \quad (16)$$

where $\Phi_{\mathrm{dif}}(f_a) = \Phi(f_a) - \Phi_{\mathrm{ref}}(f_a)$ represents the phase difference between a nonreference target and the reference target

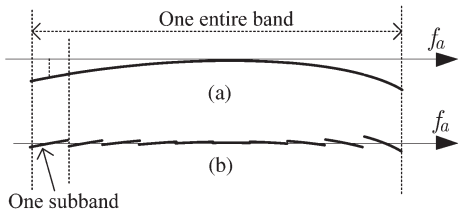

Fig. 5. (a) Remaining quadratic phase error in one entire band or a full aperture and (b) residual phase or error in each subband after phase compensation in each subband individually.

in one entire frequency band. Since the matched filter is based on the reference target, a well-matched signal from the target is obtained after the filtering. However, because $\Phi(f_a)$ of (14) is azimuth variant, the signals of the nonreference targets in (16) can be mismatched. To see the mismatched phase clearly, we expanded (16) as

$$s_{aft\_mat}(f_a) = W_{az}(f_a)\exp\left(jB_0 + j\Phi(0) - j2\pi f_a\alpha_{scl}t_c\right) \times \exp\left(j\left(\frac{\pi^2}{B_{2_0}} + \frac{\Phi''(0)}{2}\right)f_a^2 + j\xi\right) \quad (17)$$

where ξ represents the phase variation from the third-order and higher order terms. For the reference point, the coefficient of the second-order phase in (17) is zero, and the target is well matched. However, a quadratic phase term remains for nonreference targets. To compensate for the remaining quadratic phase error, a method including the division of the total azimuth frequency band into subbands, compensation for the azimuth variant in each subband, and subband synthesis is studied. The basic principle is shown in Fig. 5. The remaining quadratic phase error [Fig. 5(a)] is divided and compensated for each subband. After the compensation, the middle value of the phase in each subband is 0 [Fig. 5(b)].

Let $f_a = f_{\rm sub} + f_b$, with $f_{\rm sub}$ being the frequency in one subband and f_b being the block frequency. Then, the signal of (17) becomes

$$s_{\rm sub}(f_{\rm sub}, f_b) = s_{aft\_mat}(f_{\rm sub} + f_b). \quad (18)$$

By performing an IFFT to (18) with $f_{\rm sub}$, the signal of each target is focused. Having focused the signal in each subband, one can compensate for the error of each azimuth target within one range cell using

$$H_{\rm sub,phi}(t, t_{\rm sub}, f_b) = \exp\left(-j\left(\frac{\pi^2}{B_{2_0}} + \frac{\Phi''(0)}{2}\right)f_b^2\right). \quad (19)$$

After the compensation, the azimuth residual phase is small, as shown in Fig. 5(b). Then, the signal is retransformed into the subband frequency domain and is integrated into a full band signal. At this time, the integrated signal can be expressed by (17) without the quadratic phase term. Then, the signal is focused after an IFFT and can be written as

$$s_{in}(t_a) = \mathrm{sinc}(t_a - \alpha_{scl}t_c)\exp\left(jB_0 + j\Phi(0)\right). \quad (20)$$

From the compensation processing, one notes that the division of subband should ensure the residual jagged phase error [Fig. 5(b)] to be small enough (such as within $\pm\pi/4$). In this case, the defocus in each subband is small and can be ignored. In Section IV-C, the division of the subband will be discussed.

D. Correction for Image Distortion Caused by Range Offset

Range offset, $t_{\rm con}$ in (8), was omitted in Section III-C. The offset causes image distortion and is a known function of the zero-Doppler times of different azimuth points. Therefore, a correction function can be utilized to compensate for the distortion in the range-frequency domain. The function can be written as

$$H_{cid}(f_r, t_a) = \exp(j2\pi f_r t_{\rm con}). \quad (21)$$

In (21), $t_{\rm con}$ is a function of t_c. t_c is determined by $\mathrm{sinc}(t_a - \alpha_{scl}t_c)$ of (20), i.e., $t_c = t_a/\alpha_{scl}$.

IV. Implementation Considerations

A. Slant Range Model of the Third-Order Terms for RCM Correction

As long as a satisfactory RCM correction at the scale of one range cell resolution is achieved, the range model of (1) with the lowest possible order terms should be used. Four models of the third-, fourth-, fifth-, and sixth-order terms have been separately studied in simulations with parameters of Table I. In a simulated scene, five targets (0–4) have the same nearest range and are located within one synthetic aperture [Fig. 6(a)]. Target 0 is selected as the reference target. The azimuth offsets (away from the reference target) in time from targets 1 to 4 increase.

Along ground track between 0 and 12 h [Fig. 1(a)] and at an increment of 1 h from the targets with each model, range errors were assessed. The errors varied along the track. At the same geographic location, the error decreased when the order of terms in the model increased. For the model of the same order terms, 1) the least error was observed at 0-h location, but the largest error occurred near 4-h location, and 2) the least error was obtained from the reference target [target 0 in Fig. 6(a)], but the error from the nonreference targets [targets 1–4 in Fig. 6(a)] increased with the increase of azimuth offset. For example, Fig. 6(b) showed the error from the slant range model with only up to the third-order terms for one synthetic aperture varying from -420 to 420 s at the geographic location near 4 h [Fig. 1(a)]. The error of the reference target was the smallest, whereas the error of target 4 was the largest. The largest error was about 5 m, which is larger than one-half of a range cell resolution. Thus, in this maximum azimuth-variant case, the azimuth-variant range model up to the third-order terms was only adequate for the RCM correction of targets 0–3. Also, if the errors of the targets (-4 to -1) at the left side of the reference target were individually simulated, the errors of the targets would be the same as those of targets 1–4, respectively. It should be noted that, in the simulation, coefficients k_2 and k_3 of the third-order model were approximated as linear functions of the azimuth time. Using this approximation, we included higher order terms with respect to A_3 and A_4 of (3.a) in the removal of the azimuth variant of k_2 and k_3 as expressed in (A.6).

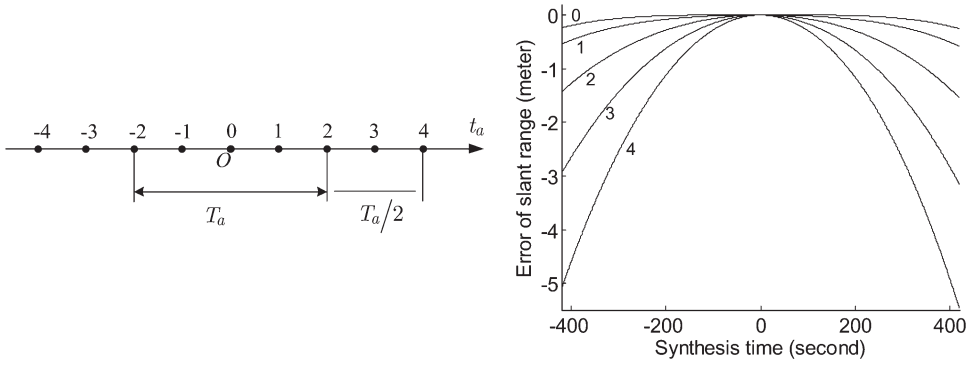

Fig. 6. (a) Layout of simulated targets in azimuth-time domain. (b) Errors using the slant range model up to the third-order terms.

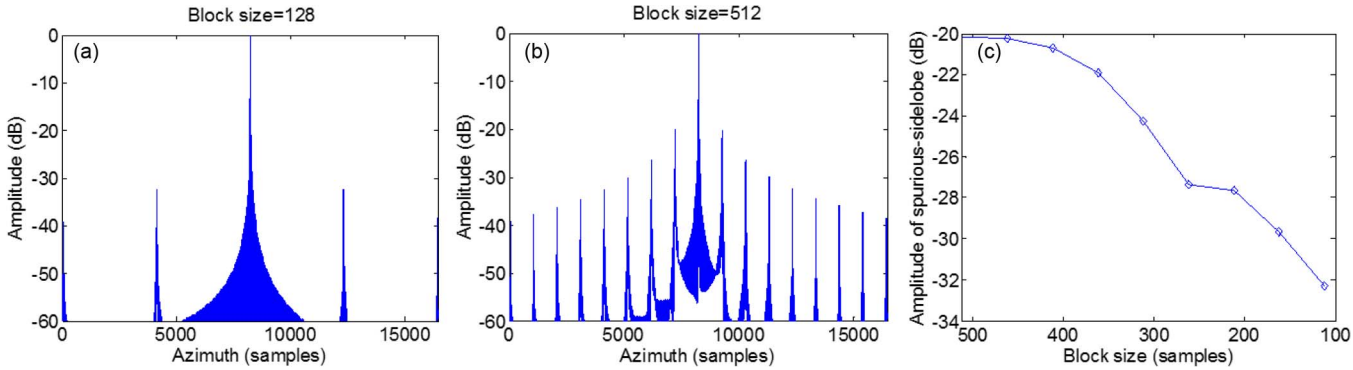

Fig. 7. Focused signal at the middle in azimuth and the grating lobes at block sizes of (a) 128 and (b) 512. The amplitude of the first grant lobe as a function of the block size (c).

B. Slant Range Model With the Sixth-Order Terms to Compensate for Phase Error

Phase error $\Delta\phi = 4\pi\Delta R_{\rm mod}/\lambda$ caused by the range error of $\Delta R_{\rm mod}$ of a range model has been evaluated in the determination of the order terms. For a satisfactory compensation, the error is generally required to be within $\pm\pi/4$ or $\pm\lambda/8$. Since the wavelength (Table I) is 0.09 m, the acceptable error in range is about 0.01 m. By simulation, the error of the slant range model with up to third-order terms is found to be far beyond 0.01 m and is not acceptable. A slant range model with higher order terms is examined. The phase errors for the range models with the sixth-order terms at 0–12 h with inclination angles from 30° to 60° were evaluated. The simulated maximum phase errors caused by the range errors were all within $\pm\pi/4$. Thus, the model with up to the sixth-order terms could adequately represent the instantaneous slant range.

C. Bandwidth of Azimuth Subbands

The subband division is the key in achieving successful azimuth focusing. The narrower the subband width is, the smaller the residual phase error after the phase compensation in each subband is, and the better the focusing is. However, as the width decreases, the number of subbands increases. Consequently, the computational efficiency could suffer. There is a trade-off between the acceptable result in focusing and computational load. After the phase compensation for the quadratic phase term of (18) in each subband, a jagged phase error remains in each subband [Fig. 5(b)]. The selection of the bandwidth of each subband should ensure that the jagged phase error is smaller than a threshold (e.g., $\pi/4$). Thus, the defocusing caused by the error can be ignored. The phase error determines the bandwidth. After phase compensation, the residual quadratic phase error can be approximated as

$$\varphi_{\rm err} = \left(\frac{\pi^2}{B_{2_0}} + \frac{\Phi''(0)}{2}\right) f_{\rm sub}^2 \triangleq A_{\rm err} f_{\rm sub}^2 \qquad (22)$$

with

$$A_{\rm err} = \frac{\pi^2}{B_{2_0}} - \frac{\pi^2}{B_2} + \sum_{n=3}^{6} \frac{n(n-1)B_n}{2B_2^n}\pi^n \left(-\frac{B_1}{2\pi}\right)^{n-2}. \qquad (22.a)$$

To ensure a well-focused result, one should confine the quadratic phase error within $\pm\pi/4$ in each subband. Thus, the bandwidth or sampling number of each azimuth subband should satisfy

$$B_{\rm sub} \le \sqrt{\frac{\pi}{\max\{A_{\rm err}\}}} \quad \text{or} \quad M_{\rm sub} \le \frac{M}{\rm PRF}\sqrt{\frac{\pi}{\max\{A_{\rm err}\}}}. \qquad (23)$$

D. Suppression of Unwanted Grant Lobes

The subband division and synthesis create the needed focused signal in azimuth but unfortunately the unwanted grating lobes. The formation of the lobes is caused by the residual of periodical phase error after the phase error compensation in each subband. The error must be within $\pm\pi/4$ to ensure well-focused results in azimuth synthesis. Furthermore, the lobes can be large in amplitudes and are located on both sides of the focused signal in azimuth uniformly [Fig. 7(a) and (b)]. The larger

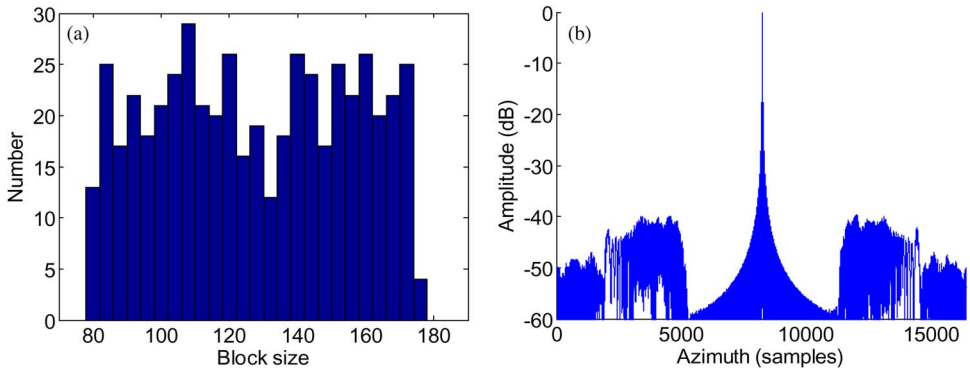

Fig. 8. (a) Histogram of randomly selected block sizes. (b) Focused signal and suppressed grant lobes in azimuth.

the number of subbands or block size, the more the number of the lobes. Also, as the block size increases, the first and subsequential lobes move closer to the focused signal, and the amplitudes increase [Fig. 7(b), cf., Fig. 7(a)]. Equivalently, as the block size decreases, the amplitudes of the first lobes are suppressed [Fig. 7(c)] so are the subsequential lobes. However, reduction in block size increases the bandwidth of each subband in which the phase error might be beyond the acceptable threshold of the compensation for the phase error. An alternative is sought to avoid this problem.

The replacement of the constant number of block size with the random number of block sizes can interrupt the periodical characteristics of the phase errors. Instead of the formation of focused error energy at fixed azimuth locations (to form distinguished grating lobes), the energy is spread. An equivalent reduction in amplitudes of the lobes occurs. Simulated results with the random number of block sizes in subbands were given. Fig. 8(a) was the histogram of the random block sizes. The focused signal and grating lobes were depicted in Fig. 8(b). There was a significant reduction in amplitudes of the lobes in Fig. 8(b) as compared to those in Fig. 7(a) and (b).

E. Computational Load

In the SV-CSA, six range FFTs, four azimuth FFTs, eight multiplications, and two subband azimuth FFTs are utilized. Therefore, the total computational load can be expressed as $3MN\log_2 N + 2NM\log_2 M + 8MN + NM\log_2 M_{\text{sub}}$, with M being the number of azimuth samples, N being the number of range samples, and M_{sub} being the number of azimuth samples in one subband. In comparison, of the BPA (e.g., [13]), for each pixel in the final image, a signal vector with a length of M is extracted from range compressed data, multiplied with a phase function, and summed. Thus, the computational load can be expressed as M^2N. In a standard CSA (e.g., [14]), two range FFTs, two azimuth FFTs, and three multiplications are used. Therefore, the computational load can be expressed as $MN\log_2 N + NM\log_2 M + 3MN$. Clearly, the BPA has the highest computational load. The load of the SV-CSA is slightly heavier than that of the CSA. Ratios of the SV-CSA to CSA and BPA to CSA at five azimuth sample sizes are computed to quantify the comparison (Table II).

TABLE II
COMPUTATIONAL LOAD ANALYSIS USING CSA AS REFERENCE

Data size in azimuth ($\times 10^4$)	1	2	4	8	16
SV-CSA/CSA ratio	2.82	2.80	2.78	2.77	2.75
PBA/CSA ratio	338.12	633.40	1191.35	2248.74	4258.10

TABLE III
SECOND SET OF SIMULATION PARAMETERS

Orbit height	36,000,000 m	Signal bandwidth	40 MHz
Inclination angle	60°	Sampling rate	48 MHz
Wavelength	0.09 m	Center time location	3:48 (hour:minute)
Antenna size	40 m	Synthesis time	840 second
Off-nadir angle	3°	PRF	140Hz

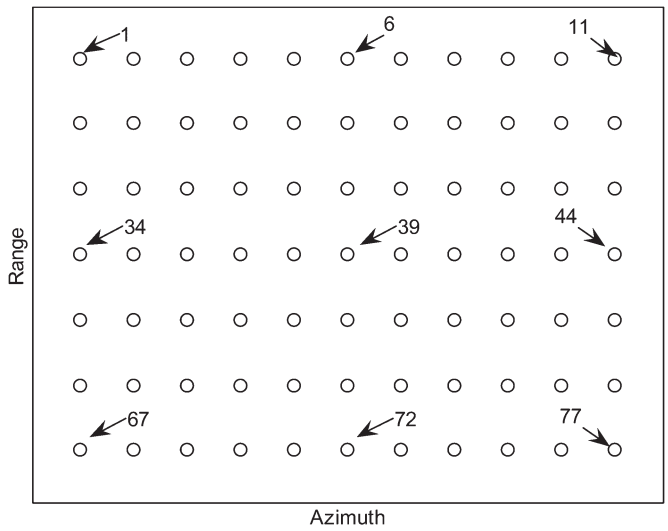

Fig. 9. Targets are uniformly distributed in the zero-Doppler azimuth time. Targets per row have the same nearest slant range.

V. VALIDITY AND APPLICABILITY

A. Assessment of RCM Equalization

The simulation parameters for the assessment were given in Table III. Point targets of 7 × 11 (row × column) were set on the ground of about 95 000 × 82 000 m (azimuth × ground range). They were uniformly distributed at zero-Doppler azimuth time. The targets by row had the same nearest slant range. They were indexed from 1 to 77 row by row (Fig. 9). The target in the middle per row was selected as the reference target of

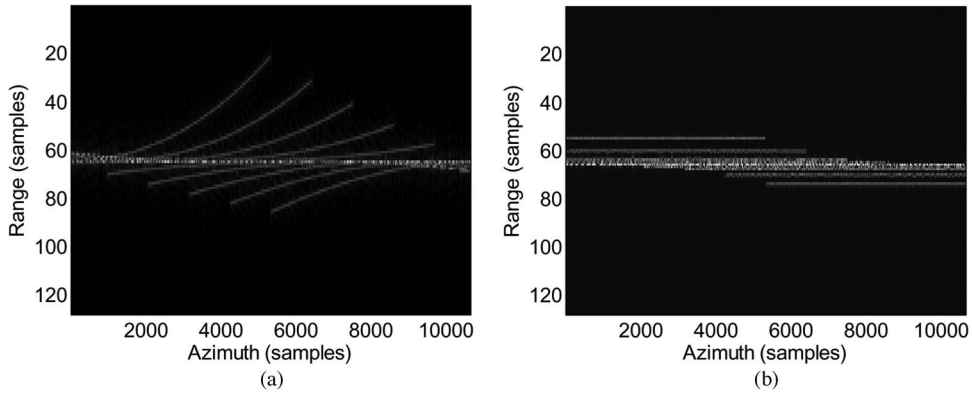

Fig. 10. Signals of targets 34–44 of row four after RCM correction. (a) Without and (b) with the RCM equalization procedure.

that row. For example, target 6 was the reference target of row one. The simulated RCMs of azimuth targets per row differed because the curvature of each RCM curve varied. Thus, row by row, the RCMs of the nonreference azimuth targets remained after using a uniform RCM correction function derived from the reference target. As an example, 11 RCM curves of targets 34–44 (row four, Fig. 9) were shown in Fig. 10(a). The curves were produced after the uniform RCM correction (or without the RCM equalization) and range compression. Each curve represented one target. The range migration of each RCM curve (after the uniform RCM correction) could be over tens of range cells. However, after the RCM equalization, the RCMs were of the same or similar forms in curvature and were corrected [Fig. 10(b)] by a uniform RCM correction function. Therefore, the azimuth signal from each target per row was focused individually in range. It should be noted that the range offset of each target was observed [Fig. 10(b)], and the offset was caused by the RCM equalization procedure. In the figure, the maximum offset away from the reference target was about ten samples of range resolution.

B. Evaluation of Residual Phase Error and Focusing

Residual phase errors of 77 targets after phase error compensation in subbands were assessed. The errors were within $\pm\pi/4$ overall. Errors of target 34 were evaluated according to its position and slant range history by numerical evaluation. Of the azimuth samples within each subband, they were between -0.2 and 0.2 rad (Fig. 11). Due to the large number of subbands, the residual errors looked solid within the azimuth samples. To closely examine the errors, we amplified the errors of subbands near the center highlighted by a circle and showed them in a rectangle insertion. The pattern of residual errors replicated roughly the pattern illustrated in Fig. 5(b).

A focused signal and grating lobes were obtained for each target after the subband synthesis. The random number of block sizes for subband division was employed to suppress the lobes. The block sizes varied approximately from 100 to 160. Focused signals from 77 targets were simulated. Satisfactory results were achieved. As an example, impulse responses shown as contours from targets 1, 6, 11, 34, 39, and 44 were plotted (Fig. 12). The targets were visually well focused. Two observations were noted (Fig. 12). The range sidelobes of the targets on the first and third columns were tilted in azimuth. The cause was that the synthesis center of the imaging geometry [Fig. 1(a)] was at 3 : 48 (Table I). Of the tilted lobes, the imaging geometry of the targets was similar to that of a spotlight SAR. Also, the acquisition time in the simulation was about 1.2 times that of one full synthetic aperture in length. The target at the center location per row was illuminated with the longest time. Thus, the azimuth resolution was the highest for the target at the center and decreased as the targets moved away from the center.

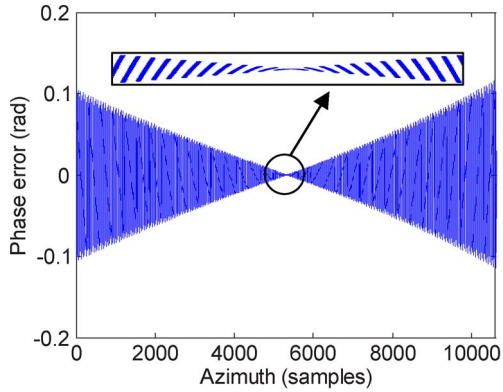

Fig. 11. Residual phase error of target 34 after the phase error compensation in subbands. The errors of the subbands near the center circle were amplified and showed within a rectangle insertion.

The values of the peak sidelobe ratio (PSLR) and integral sidelobe ratio (ISLR) of the targets are further computed to quantify the degree of focusing. The PSLR is the ratio of the maximum peak value to the maximum sidelobe peak value. The ISLR is defined as

$$\mathrm{ISLR} = 10\log_{10}\left(\frac{P_{\mathrm{total}} - P_{\mathrm{main}}}{P_{\mathrm{total}}}\right) \tag{24}$$

where P_{total} is the total signal energy and P_{main} is the energy of the signal within the first zero points. For a theoretically well-focused signal of an ideal sinc function, the PSLR and ISLR are -13.26 and -10.26 dB, respectively. In comparison with the theoretical values, well-focused results are obtained (Table IV).

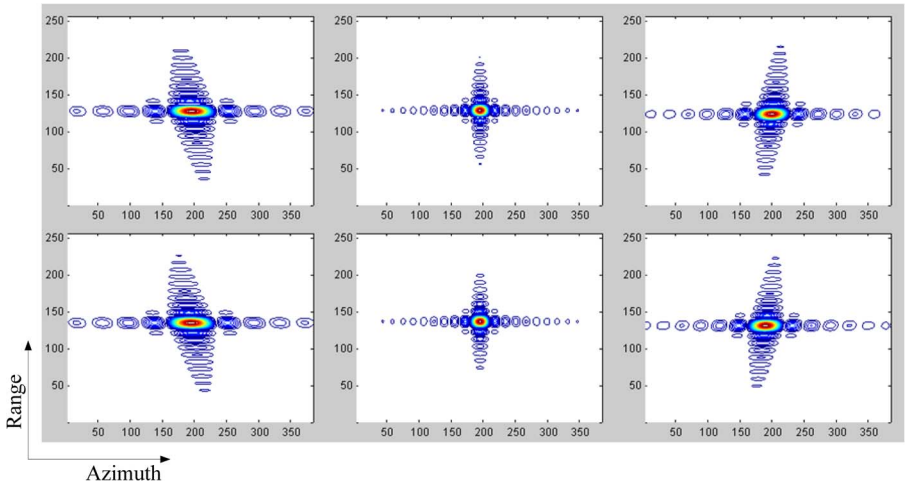

Fig. 12. Impulse responses shown as contours of azimuth compressed targets 1, 6, and 11 from left to right in row one and 34, 39, and 44 from left to right in row two.

TABLE IV
SIMULATED VALUES OF PSLR AND ISLR

	Range		Azimuth	
Targets	PSLR(dB)	ISLR(dB)	PSLR(dB)	ISLR(dB)
1	–13.27	–9.97	–13.32	–10.42
6	–13.35	–10.58	–13.25	–9.94
11	–13.25	–10.00	–13.29	–10.23
34	–13.30	–10.43	–13.28	–10.51
39	–13.38	–10.72	–13.25	–9.96
44	–13.30	–10.49	–13.25	–10.26

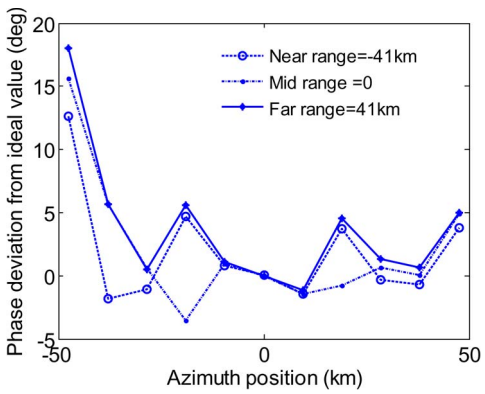

Fig. 13. Phase deviation off an ideal value for targets 1–11, 34–44, and 67–77 at near, middle, and far ranges, respectively.

To further understand the phase preservation of the proposed method [26], we computed the phase deviations of targets 1–11, 34–44, and 67–77 from its ideal value (20), respectively. The deviations were generally within or around $\pm 5^\circ$ (Fig. 13) except for targets 1, 34, and 67 that are at azimuth edge (Fig. 9).

C. Constraint on the Spatial Extent Along Azimuth and Range Dimensions

As the extent expands, the degree of azimuth-variant or range-variant increases. Because of the large azimuth-variant RCM, the difference of RCMs from azimuth targets within one range cell can be up to several range resolution cells. Thus, the difference cannot be ignored. $\varepsilon(f_a)$ in (A.4) is the coefficient of the azimuth-variant RCM. With the studied RCM equalization, the second- and third-order terms of $\varepsilon(f_a)$ are removed, but the fourth-order and higher order terms remain. Since the azimuth-variant RCM from the fourth-order term should dominate the azimuth-variant RCM ($\Delta R_{\mathrm{rcm},a}$) after the equalization, $\Delta R_{\mathrm{rcm},a}$ can be approximately evaluated by the term as

$$\Delta R_{\mathrm{rcm},a} = \left| \frac{3\pi^3 D_{4_0}}{4D_{2_0}^4} \left(\frac{D_{4_1,t_c}}{D_{4_0}} - 4\frac{D_{2_1,t_c}}{D_{2_0}} \right) \frac{f_a^4}{\lambda} t_c \right|. \quad (25)$$

Usually, the residual RCMs must be less than or equal to a fraction (e.g., 0.5) of a range resolution cell to be ignored. With the consideration of $|f_a| \le B_a/2$, where B_a denotes the azimuth bandwidth and the combination with (25), the allowable azimuth time is

$$|t_c| \le \frac{\rho_r/2}{\left| \frac{3\pi^3 D_{4_0}}{64\lambda D_{2_0}^4} \left(\frac{D_{4_1,t}}{D_{4_0}} - 4\frac{D_{2_1,t}}{D_{2_0}} \right) B_a^4 \right|} \quad (26)$$

where ρ_r is the range resolution. Of the simulated example (Table IV), the time was from -841 to 841 s at $\rho_r = 3.75$ m.

The RCM that is range variant is typically expressed as the first-order and higher order terms in a polynomial in range dimension as well. The CS algorithm can only adequately handle the range-variant RCM of the first-order term. Thus, the range signal of a processed imaging scene should be limited, or the subdivision of the scene into narrow strips is required to ensure that the second-order and higher order range-variant RCMs in each strip are small enough to be ignored. Also, the range-variant RCM from the second-order term contributes the most in the range-variant RCM ($\Delta R_{\mathrm{rcm},r}$) after the RCM correction. Thus, $\Delta R_{\mathrm{rcm},r}$ can be approximately assessed by

$$|\Delta R_{\mathrm{rcm},r}| = \left| \frac{c\pi D_{2_1,r}^2}{4D_{2_0}^3} \frac{f_a^2}{f_c} \left(\frac{r}{2} \right)^2 \right| \quad (27)$$

and it should also be confined by half a range resolution, i.e., $\rho_r/2$. Thus, one obtains

$$|r| \le \sqrt{\frac{32\rho_r D_{2_0}^3}{\left|\lambda\pi D_{2_1,r}^2 B_a^2\right|}}. \tag{28}$$

With simulation parameters in Table III, the range extent in each narrow strip was from $-55\,750$ to $55\,750$ m at $\rho_r = 3.75$ m.

So far, the GEO-SAR is discussed under the strip-mapping mode. If a fine resolution is preferred, the spotlight SAR mode can be considered. Because of the increased range resolution, the current range model up to the third-order terms may not be accurate enough. The fourth-order or higher order terms should be used. On the other hand, the level of azimuth variant weakens since the extent of illuminated scene decreases. Thus, the current strategies of the RCM equalization, subband division and subband synthesis, and random selection of subband block size can be used without any modification. If a wide swath is expected, the ScanSAR mode can be adopted. In this mode, the range resolution is coarser than the one that the current model can adequately handle. No change to the current range model is needed. As compared to the azimuth synthesis of the current model, the time in the ScanSAR mode is shortened. Thus, the azimuth variant should be weakened. The current method can be directly applied to the ScanSAR mode in azimuth processing as well.

VI. Conclusion

Long integration time of a synthetic aperture and highly nonlinear orbit geometry are two unique characteristics of the GEO-SAR. Of the imaging geometry, the RCMs and phase error are range and azimuth variant or 2-D space variant. Traditional azimuth-invariant imaging algorithms in the RD domain cannot be directly applicable in the processing of GEO-SAR data since the space-variant RCMs and azimuth-variant phase error cannot be satisfactorily corrected. Thus, a 2-D SV-CSA based on the RCM equalization and subband synthesis has been studied. After the RCM equalization, the space-variant RCMs became approximately space invariant at the scale of one range cell resolution. Thus, the RCMs were corrected with a uniform RCM correction function derived from a reference target within the range cell. Because the wavelength was usually much smaller than the range cell resolution, the range error at the scale of a fraction (e.g., 1/8) of a wavelength could still remain. The result was the existence of phase error. To compensate for the azimuth-variant phase error that is required to be within $\pm\lambda/8$ for a satisfactory focus in azimuth, we have further divided the azimuth signal of each range cell or the signal of an entire band into subbands. In each subband, the variation of the phase error was much smaller than $\pi/4$ and could be ignored. Thus, the phase error was considered as azimuth invariant. After the compensation for error in each subband, a subband synthesis was performed to form the signal for the entire band. Consequently, the 2-D space-variant signal of the GEO-SAR was processed. The validity of proposed algorithm was evaluated through the analysis of simulated GEO-SAR data from targets distributed in a large ground scene. There was a clear separation of the mainlobe and the first and subsequential sidelobes from the contours of impulse responses of the targets. The computed PSLR and ISLR values quantified the satisfactory results.

Appendix A
$\tau(R_b, f_a)$, A_3, and A_4

Using the definition of D_n and (3.a), one could express D_2 and D_3 as

$$\begin{aligned} D_2 &= -\frac{4\pi}{\lambda}\left(k_2 + 3A_3 t_c + 6A_4 t_c^2\right) \\ D_3 &= -\frac{4\pi}{\lambda}(k_3 + A_3 + 4A_4 t_c). \end{aligned} \tag{A.1}$$

Since k_n $(n = 2, 3, 4, \ldots)$ are space variant, they can be expanded and then approximated in range and azimuth time as

$$k_n \approx k_{n_0} + \frac{\partial k_n}{\partial r} r + \frac{\partial k_n}{\partial t_c} t_c \triangleq k_{n_0} + k_{n_1,r} r + k_{n_1,t_c} t_c \tag{A.2}$$

where k_{n_0} is a space-invariant term. $r = R_b - R_{\text{ref}}$. $rk_{n_1,r}$ is the first-order term of the range variant. $t_c k_{n_1,t_c}$ is the first-order term of the azimuth variant. Inserting (A.2) to (A.1), one could express D_n as a series of r and t_c

$$D_n \approx D_{n_0} + \frac{\partial D_n}{\partial r} r + \frac{\partial D_n}{\partial t_c} t_c \triangleq D_{n_0} + r D_{n_1,r} + t_c D_{n_1,t_c} \tag{A.3}$$

where D_{n_0} is the zero-order term of D_n. $D_{n_1,r}$ and D_{n_1,t_c} are the first-order partial derivatives of D_n related to r and t_c, respectively. Then, $\tau(R_b, f_a)$ in (4.b) can be approximately expressed as

$$\tau(R_b, f_a) \approx t_0 + t_{\text{con}}(t_c) + \alpha(f_a) + \beta(f_a) r + \varepsilon(f_a) t_c \tag{A.4}$$

with

$$t_0 = 2R_b/c \tag{A.4.a}$$

$$t_{\text{con}}(t_c) = 2r_0/c \tag{A.4.b}$$

$$\alpha(f_a) = -\frac{\pi}{2D_{2_0}}\frac{f_a^2}{f_c} + \sum_{n=3}^{6}(n-1)\frac{\pi^{n-1}D_{n_0}}{2D_{2_0}^n}\frac{f_a^n}{f_c} \tag{A.4.c}$$

$$\begin{aligned} \beta(f_a) = &-\frac{\pi}{2D_{2_0}}\left(-\frac{D_{2_1,r}}{D_{2_0}}\right)\frac{f_a^2}{f_c} \\ &+ \sum_{n=3}^{6}(n-1)\frac{\pi^{n-1}D_{n_0}}{2D_{2_0}^n}\left(\frac{D_{n_1,r}}{D_{n_0}} - n\frac{D_{2_1,r}}{D_{2_0}}\right)\frac{f_a^n}{f_c} \end{aligned} \tag{A.4.d}$$

$$\begin{aligned} \varepsilon(f_a) = &-\frac{\pi}{2D_{2_0}}\left(-\frac{D_{2_1,t_c}}{D_{2_0}}\right)\frac{f_a^2}{f_c} \\ &+ \sum_{n=3}^{6}(n-1)\frac{\pi^{n-1}D_{n_0}}{2D_{2_0}^n}\left(\frac{D_{n_1,t_c}}{D_{n_0}} - n\frac{D_{2_1,t_c}}{D_{2_0}}\right)\frac{f_a^n}{f_c} \end{aligned} \tag{A.4.e}$$

where t_0 is the round-trip time from the nearest slant range. $t_{\text{con}}(t_c)$ denotes a range offset caused by the use of the range perturbation function in the RCM equalization [Fig. 4(c)].

$\alpha(f_a)$ is the RCM at reference range, $\beta(f_a)$ is a range factor of the RCM, and $\varepsilon(f_a)$ is an azimuth factor of the RCM. In (A.4), the second- and high-order terms of slant range are omitted, and they are considered as a limitation on range swath as shown in (28) (Section V-C). If the limitation is not satisfied, the subdivision of the scene into narrow strips is required. $\alpha(f_a)$, $\beta(f_a)$, and $\varepsilon(f_a)$ are space invariant. If $\varepsilon(f_a)$ is not equal to 0, the RCMs of the reference and nonreference targets differ. Then, a uniform RCM correction cannot correct all of the RCMs simultaneously as shown (Fig. 4). Therefore, to make $\varepsilon(f_a)$ as close to zero as possible, one can set its major components that are the second- and third-order terms to zeros or

$$D_{2_1,t_c} = 0 \quad D_{3_1,t_c}/D_{3_0} - 3D_{2_1,t_c}/D_{2_0} = 0. \tag{A.5}$$

Inserting (A.1)–(A.3) to (A.5), one obtains

$$A_3 = -k_{2_1,t_c}/3 \quad A_4 = -k_{3_1,t_c}/4. \tag{A.6}$$

Appendix B
Range CS

It is desirable to develop and implement a CS function that is space invariant [14]. For the GEO-SAR, the equivalent frequency-modulated rate γ_e is of weak range variant within an illuminated scene after a close-up examination. If the difference of γ_e at the reference line and the nearest line satisfies

$$\Delta\gamma_e \le \gamma_{e^2}/B^2 \tag{B.1}$$

the resulting phase error of the traditional scaling function is confined within $\pm\pi/4$. In this case, the residual phase will not cause unacceptable defocusing in range after range compression. $\Delta\gamma_e$(B.1) can be approximately computed by using (4.c) and (A.3) as

$$\Delta\gamma_e \approx \frac{\pi}{D_{2_0}}\frac{D_{2_1,r}}{D_{2_0}}\frac{f_a^2}{f_c^2}r \tag{B.2}$$

where r is the range offset of the point target to the reference line. Inserting (B.2) to (B.1), one can obtain

$$r \le \frac{\gamma_{e^2}}{\pi B^2}\frac{D_{2_0}^2 f_c^2}{D_{2_1,r} f_a^2}. \tag{B.3}$$

Once (B.3) is satisfied, the equivalent frequency-modulated rate can be regarded as range invariant and approximated as

$$\frac{1}{\gamma_e} \approx \frac{1}{\gamma} + \frac{\pi}{D_{2_0}}\frac{f_a^2}{f_c^2} - \sum_{n=3}^{6} n(n-1)\frac{\pi^{n-1}D_{n_0}}{2D_{2_0}^n}\frac{f_a^n}{f_c^2}. \tag{B.4}$$

Thus, D_n $(n = 2, 3, 4, 5, 6)$ of space variant are replaced with D_{n_0} $(n_0 = 2, 3, 4, 5, 6)$ of space invariant, respectively.

Appendix C
E_i $(i = 2, 3, 4, 5)$, Y_3, and α_{scl}

In (12.a), E_2 is the azimuth scaling coefficient, and E_i $(i = 3, 4$ or $5)$ is a coefficient to weaken the azimuth variation in B_{i-1} $(i = 3, 4$ or $5)$. To minimize the variation, one sets $\partial B_{i-1}/\partial t_c = 0$ $(i = 3, 4,$ and $5)$. Applying them to (12.a), one obtains

$$\begin{cases} E_3 = -k_{2_1}/3 \\ E_4 = -\left(k_{3_1} + 3Y_3 D_{2_0}^2 D_{2_1,t}\right)/4 \\ E_5 = -k_{4_1}/5. \end{cases} \tag{C.1}$$

To solve E_2 and Y_3, we then analyze the image distortion along azimuth direction by expanding $\Phi(f_a)$ in (14) as

$$\Phi(f_a) = \Phi(0) + \Phi'(0)f_a + \Phi''(0)f_a^2/2 + \cdots \tag{C.2}$$

with

$$\Phi'(0) = \pi\frac{B_1}{B_2} + \frac{3\pi B_3 B_1^2}{4B_2^3} + \sum_{n=4}^{6}\frac{B_n}{B_2^n}n\pi^n\left(-\frac{B_1}{2\pi}\right)^{n-1}. \tag{C.3}$$

$\Phi'(0)$ determines the azimuth position after signal focusing and is further expanded as a series of t_c

$$\begin{aligned}\Phi'(0) &= bt_c + ct_c^2 + \cdots \\ &\approx bt_c + ct_c^2\end{aligned} \tag{C.4}$$

where b represents the azimuth scaling and c is the azimuth distortion. Also, with (12.a), b and c are algebraically expressed as

$$b = \frac{2\pi E_2}{k_{2_0} + E_2} \tag{C.5}$$

$$c = \pi\frac{3E_3 - 2E_2\frac{k_{2_1}+3E_3}{k_{2_0}+E_2}}{k_{2_0}+E_2} + \pi\frac{3\left(k_{3_0}+E_3+Y_3D_{2_0}^3\right)E_2^2}{(k_{2_0}+E_2)^3}. \tag{C.6}$$

Set $b = 2\pi(1 - \alpha_{scl})$. Then, E_2 is solved as

$$E_2 = k_{2_0}\frac{1-\alpha_{scl}}{\alpha_{scl}}. \tag{C.7}$$

The value of α_{scl} is empirically determined as follows. In the phase scaling function of (11), a spectrum shifting in the azimuth-Doppler domain occurs. The shift can be evaluated by

$$\Delta f_{\text{off}} = 2E_2 t_c/\lambda. \tag{C.8}$$

This shifting results to the widening of the azimuth bandwidth. Thus, a PRF that is greater than the biggest Doppler bandwidth is required. However, the high PRF means a large number of sampling points, which could sequentially reduce computational efficiency. Therefore, Δf_{off} should be minimized. The minimization can be achieved once E_2 is chosen to approach 0 or α_{scl} is approaching 1.

Letting no distortion or $c = 0$, one can solve Y_3 as

$$Y_3 = -\frac{1}{D_{2_0}^3}\left(3E_3 - 2E_2\frac{k_{2_1}+3E_3}{k_{2_0}+E_2}\right)\frac{(k_{2_0}+E_2)^2}{3E_2^2} - \frac{1}{D_{2_0}^3}(k_{3_0}+E_3). \tag{C.9}$$

Finally, with $\Phi'(0)$ consisting of only the first-order term of bt_c, (C.2) is rewritten as

$$\Phi(f_a) = \Phi(0) + 2\pi(1-\alpha_{scl})t_c f_a + \Phi''(0)f_a^2/2 + \cdots. \tag{C.10}$$

REFERENCES

[1] W. Pitz and D. Miller, "The TerraSAR-X satellite," *IEEE Trans. Geosci. Remote Sens.*, vol. 48, no. 2, pp. 615–622, Feb. 2010.

[2] J. H. González, M. Bachmann, R. Scheiber, and G. Krieger, "Definition of ICESat selection criteria for their use as height references for TanDEM-X," *IEEE Trans. Geosci. Remote Sens.*, vol. 48, no. 6, pp. 2750–2757, Jun. 2010.

[3] T. Toutin, "Radarsat-2 DSM generation with new hybrid, deterministic, and empirical geometric modeling without GCP," *IEEE Trans. Geosci. Remote Sens.*, vol. 50, no. 5, pp. 2049–2055.

[4] K. Tomiyasu, "Conceptual performance of a satellite borne, wide swath synthetic aperture radar," *IEEE Trans. Geosci. Remote Sens.*, vol. GRS-19, no. 2, pp. 108–116, Apr. 1981.

[5] K. Tomiyasu and J. L. Pacelli, "Synthetic aperture radar imaging from an inclined geosynchronous orbit," *IEEE Trans. Geosci. Remote Sens.*, vol. GRS-21, no. 3, pp. 324–329, Jul. 1983.

[6] D. Bruno, S. E. Hobbs, and G. Ottavianelli, "Geosynchronous synthetic aperture radar: Concept design, properties and possible applications," *Acta Astronautica*, vol. 59, no. 1-5, pp. 149–156, Sep. 2006.

[7] W. Sheng and S. E. Hobbs, "Research on compensation of motion, Earth curvature and tropospheric delay in GEOSAR," *Acta Astronautica*, vol. 68, no. 11/12, pp. 2005–2011, Jun./Jul. 2011.

[8] S. N. Madsen, W. Edelstein, L. D. DiDomenico, and J. LaBrecque, "A geosynchronous synthetic aperture radar for tectonic mapping, disaster management and measurements of vegetation and soil moisture," in *Proc. IEEE IGARSS*, Jul. 2001, vol. 1, pp. 447–449.

[9] S. N. Madsen, C. Chen, and W. Edelstein, "Radar options for global earthquake monitoring," in *Proc. IEEE IGARSS*, Jun. 2002, vol. 3, pp. 1483–1485.

[10] C. Prati, F. Rocca, D. Giancola, and A. M. Guarnieri, "Passive geosynchronous SAR system reusing backscattered digital audio broadcasting signals," *IEEE Trans. Geosci. Remote Sens.*, vol. 36, no. 6, pp. 1973–1976, Nov. 1998.

[11] D. Bruno and S. E. Hobbs, "Radar imaging from geosynchronous orbit: Temporal decorrelation aspects," *IEEE Trans. Geosci. Remote Sens.*, vol. 48, no. 7, pp. 2924–2929, Jan. 2010.

[12] C. Hu, T. Long, T. Zeng, F. Liu, and Z. Liu, "The accurate focusing and resolution analysis method in geosynchronous SAR," *IEEE Trans. Geosci. Remote Sens.*, vol. 49, no. 10, pp. 3548–3563.

[13] L. Zhuo, L. Chunsheng, Y. Ze, Z. Jian, and C. Jie, "Back projection algorithm for high resolution GEO-SAR image formation," in *Proc. IGARSS*, 2011, pp. 336–339.

[14] R. K. Raney, H. Runge, R. Bamler, I. G. Cumming, and F. H. Wong, "Precision SAR processing using chirp scaling," *IEEE Trans. Geosci. Remote Sens.*, vol. 32, no. 4, pp. 786–799, Jul. 1994.

[15] A. Moreira, J. Mittermayer, and R. Scheiber, "Extended chirp scaling algorithm for air and spaceborne SAR data processing in stripmap and ScanSAR imaging modes," *IEEE Trans. Geosci. Remote Sens.*, vol. 34, no. 5, pp. 1123–1136, Sep. 1996.

[16] G.-C. Sun, M. Xing, Y. Wang, Y. Liu, Y. Zhang, Y. Wu, and Z. Bao, "A new signal model for a wideband synthetic aperture imaging sensor," *Can. J. Remote Sens.*, vol. 37, no. 2, pp. 171–183, 2011.

[17] C. Clemente and J. J. Soraghan, "Approximation of the bistatic slant range using Chebyshev polynomials," *IEEE Geosci. Remote Sens. Lett.*, vol. 9, no. 4, pp. 682–686, Jul. 2012.

[18] F. Wang and X. Li, "A new method of deriving spectrum for bistatic SAR processing," *IEEE Geosci. Remote Sens. Lett.*, vol. 7, no. 3, pp. 483–486, Jul. 2010.

[19] Y. Neo, F. Wong, and I. G. Cumming, "A two-dimensional spectrum for bistatic SAR processing using series reversion," *IEEE Geosci. Remote Sens. Lett.*, vol. 4, no. 1, pp. 93–96, Jan. 2007.

[20] D. D'Aria and A. M. Guarnieri, "High-resolution spaceborne SAR focusing by SVD-Stolt," *IEEE Geosci. Remote Sens. Lett.*, vol. 4, no. 4, pp. 639–643, Oct. 2007.

[21] I. G. Cumming and F. H. Wong, *Digital Processing of Synthetic Aperture Radar Data: Algorithms and Implementation*. Boston, MA, USA: Artech House, 2005.

[22] W. G. Carrara, R. S. Goodman, and R. M. Majewski, *Spotlight Synthetic Aperture Radar-Signal Processing and Algorithms*. Boston, MA, USA: Artech House, 1995.

[23] G. W. Davidson, I. G. Cumming, and M. R. Ito, "A chirp scaling approach for processing squint mode SAR data," *IEEE Trans. Aerosp. Electron. Syst.*, vol. 32, no. 1, pp. 121–133, 1996.

[24] G.-C. Sun, X. Jiang, M. Xing, Z. Qiao, Y. Wu, and Z. Bao, "Focus improvement of highly squinted data based on azimuth non-linear scaling," *IEEE Trans. Geosci. Remote Sens.*, vol. 49, no. 6, pp. 2308–2322, Jun. 2011.

[25] E. C. Zaugg and D. G. Long, "Generalized frequency-domain SAR processing," *IEEE Trans. Geosci. Remote Sens.*, vol. 47, no. 11, pp. 3761–3773, Nov. 2009.

[26] M. Belotti, D. D'Aria, P. Guccione, N. Miranda, A. M. Guarnieri, and B. Rosich, "Requirements and tests for phase preservation in a SAR processor," *IEEE Trans. Geosci. Remote Sens.*, to be published.

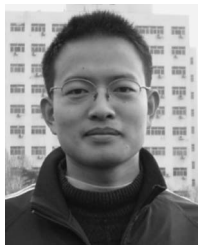

Guang-Cai Sun (M'13) was born in Hubei, China, in December 1984. He received the B.Sc. degree in communications engineering from Post and Telecommunication Institution, Xi'an, China, in 2006 and the Ph.D. degree in electrical engineering from Xidian University, Xi'an, China, in 2012.

He is currently a Researcher with the National Laboratory of Radar Signal Processing, Xidian University, Xi'an. He is the author or coauthor of 1 book and has published over 40 papers. His research interests include imaging of several synthetic aperture radar modes and moving target detection and imaging.

Mengdao Xing (M'04) was born in Zhejiang, China, in November 1975. He received the B.S. and Ph.D. degrees in electrical engineering from Xidian University, Xi'an, China, in 1997 and 2002, respectively.

He is currently a Full Professor with the National Laboratory of Radar Signal Processing, Xidian University. He is also with the National Key Laboratory of Microwave Imaging Technology, Institute of Electronics, Chinese Academy of Sciences, Beijing, China. He is the author or coauthor of 2 books and has published over 200 papers. His research interests include synthetic aperture radar (SAR), inversed SAR, and sparse signal processing.

Yong Wang received the Ph.D. degree from the University of California, Santa Barbara, CA, USA, in 1992, with focus on synthetic aperture radar and its application in forested environments.

He is currently a Faculty Member with the University of Electronic Science and Technology of China, Chengdu, China, and East Carolina University, Greenville, NC, USA. His general research area is the application of remotely sensed and geospatial data sets to environments, natural hazards, and air pollution.

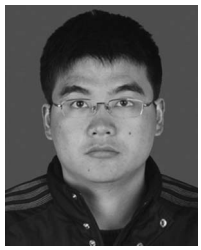

Jun Yang was born in Hubei, China, in October 1984. He received the B.Sc. degree in computer science and technology from Xi'an Institute of Posts and Telecommunications, Xi'an, China, in 2006. He is currently working toward the Ph.D. degree in the National Key Laboratory for Radar Signal Processing, Xidian University, Xi'an.

His research interests include synthetic aperture radar imaging and electronic countermeasure.

Zheng Bao (M'80–M'90–LSM'09) was born in Jiangsu, China.

He is currently a Professor with Xidian University, Xi'an, China, where he is also the Chairman of the Academic Board of the National Laboratory of Radar Signal Processing. He is the author or coauthor of 6 books and has published over 300 papers. His current research fields include space-time adaptive processing, radar imaging (synthetic aperture radar (SAR)/ISAR), automatic target recognition, and over-the-horizon-radar signal processing.